JOURNAL OF GEOPHYSICAL RESEARCH, VOL. 106, NO. A5, PAGES 8205–8216, MAY 1, 2001

Imaging the three-dimensional solar wind

Mike Gruntman

Department of Aerospace and Mechanical Engineering, University of Southern California, Los Angeles, California

Abstract. Charge exchange collisions between the solar wind alpha particles and heliospheric atomic hydrogen produce a unique emission in the 30.4-nm line. We demonstrate that an all-sky image in this emission would reveal the three-dimensional flow properties of the solar wind, including the flow properties in the regions over the Sun's poles and on the far side of the Sun. The boundary separating the fast (high-latitude) and slow (low-latitude) solar wind can be established remotely, from 1 AU. Most of the observed 30.4-nm emission would originate in the region extending up to 10 AU from the Sun. Solar wind flow velocities can be obtained both from radiance directional dependence (images) and directly from the Doppler shifts. The fast and slow solar wind flows would produce emissions spectrally separated by ~0.03 nm (~0.3 Å). The feasibility of solar wind imaging depends on the spectral properties and relative strength of the background radiation. The main background sources include galactic diffuse and stellar radiation, glow of the interstellar plasma beyond the heliopause, and glow of the solar wind pickup ions. We show that the solar wind emissions are clearly spectrally separated from the background radiation. Metastable single-charged helium ions would also be produced in the solar wind charge exchange collisions. Two-photon decay of these ions would dominate in many directions the continuum extreme ultraviolet background at 1 AU in the 30-90 nm spectral range.

1. Three-Dimensional Solar Wind

The solar wind flow is essentially three-dimensional. The Ulysses passage over the Sun's poles has provided direct experimental evidence of a strong latitudinal dependence of the flow properties [e.g., *Neugebauer*, 1999; *McComas et al.*, 2000a]. At solar minimum the polar solar wind plasma distinctly differs from the plasma flow near the solar equator or the ecliptic plane. The high-latitude solar wind is faster and less dense than the low-latitude solar wind within ±20° from the equator.

Ulysses is a unique mission that directly probes the solar wind at high latitudes. Propulsion limitations presently confine other in situ measurements to the ecliptic plane. A tilt of the Sun's effective magnetic dipole with respect to the Sun's rotation axis allows solar wind measurements at various heliomagnetic latitudes. Occasionally, even the high heliomagnetic latitude solar wind is sampled in the ecliptic. The properties of the measured solar wind essentially depend on the place of its origin at the Sun. Connecting the properties of the in situ sampled plasma with the specific features observed at the Sun's surface is of fundamental importance for understanding coronal heating and solar wind acceleration. The mechanisms of acceleration remain a major unresolved problem after 40+ years of extensive study.

The properties of the in situ sampled solar wind are influenced by the interaction between the fast and slow plasma flows. Knowledge of the distance to and shape of the boundary separating these flows is critical for interpretation of the near-ecliptic solar wind measurements. The latitudinal dependence of the solar wind properties significantly varies during the solar cycle. The anisotropy was reliably inferred from the interplanetary HI Ly α glow measurements by *Lallement et al.* [1985]. Recent observations [*Bertaux et al.*, 1996, 1999] on Solar and Heliospheric Observatory (SOHO) suggest the significantly diminished anisotropy at solar maximum. The range of solar latitudes with the slow solar wind significantly varies through the solar cycle. During its second polar orbit, Ulysses has not entered the fast solar wind at latitude at least up to −45° [*McComas et al.*, 2000b]. When did the solar wind global flow change since the first polar orbit? How fast did the change occur? Is the change symmetric with respect to heliomagnetic latitude?

Charge exchange collisions between the solar wind alpha particles (He^{2+} ions) and interstellar atomic hydrogen filling the heliosphere would produce a unique emission in the 30.4-nm line. *Paresce et al.* [1983] first pointed out that the collision product, He^{+} ions, could be in the excited $He^{+}(2p)$ state and emit 30.4-nm photons. Gruntman [1992] later estimated the brightness of this diffuse radiation ~1 mR. (1 R = 1 Rayleigh = $10^6/4\pi$ photons cm^{-2} s^{-1} sr^{-1}; 1 mR = 10^{-3} R.)

We demonstrate that an all-sky image at 30.4 nm would reveal the three-dimensional flow properties of the solar wind at the moment of observation, including the flow properties in the regions over the Sun's poles and on the far side of the Sun. In particular, the boundary separating the fast (high-latitude) and slow (low-latitude) solar wind can be established remotely, from 1 AU. Solar wind velocities can be obtained both from radiance directional dependence and directly from the Doppler shifts. The fast and slow solar wind flows would produce emissions spectrally separated by ~0.03 nm (~0.3 Å). Measurements of the interplanetary HI Ly α (121.6 nm) glow [*Lallement et al.*, 1985; *Bertaux et al.*, 1996, 1999; *Kyrölä et al.*, 1998] allow only indirect probing of the global solar wind flow pattern averaged over several years (see section 3). The

Paper number 2000JA000277.
0148-0227/01/2000JA000277$09.00

proposed solar wind imaging in the 30.4-nm emissions is much more sensitive to flow directional and temporal variations and allows direct measurements of the solar wind velocities.

Four sources would contribute to the background radiation at 30.4 nm: diffuse galactic background, stellar radiation field, glow of interstellar plasma beyond the heliopause, and glow of the solar wind pickup ions. The latter two sources are caused by scattering of the solar radiation by the interstellar and solar wind ions, respectively [*Gruntman and Fahr*, 1998, 2000; *Gruntman*, 2001]. The feasibility of solar wind imaging depends on the spectral properties and relative strength of the background radiation. We show that the collision-produced solar wind emissions are clearly spectrally separated from the background radiation at 30.4 nm. Our focus is on the study of the physical feasibility of imaging of the three-dimensional solar wind. The space mission, experiment, and instrumentation are beyond the scope of this article and only briefly discussed below.

2. 30.4-nm Emission in Charge Exchange Collisions

The concept of imaging of the three-dimensional solar wind is based on the resonance emission at 30.4 nm (more precisely 30.378 nm) produced in charge exchange of the solar wind alpha particles and heliospheric hydrogen atoms. Helium is the second most abundant component of the solar wind, and alpha particles typically constitute 4-5% of the number of plasma ions. Interstellar hydrogen atoms, the most abundant component of the neutral gas in the local interstellar medium (LISM), penetrate and fill the heliosphere.

Charge exchange collisions between alpha particles and hydrogen atoms produce protons and singly ionized helium ions:

$$He^{2+} + H \rightarrow He^{+} + H^{+}. \quad (1)$$

The ionization potential of hydrogen atoms is 13.6 eV. The ionization potentials of He^+ ions are 54.4 eV and 13.6 eV for the ground $He^+(1s)$ state and for the first excited state ($He^+(2p)$ or $He^+(2s)$), respectively (Figure 1). The $He^+(2p)$ state undergoes a rapid (~0.1 ns) transition to the ground state with emission of a 30.378-nm photon. This emission is the basis for solar wind imaging. The ionization potential of hydrogen atoms is nearly equal to that of He^+ in the first excited state. Such

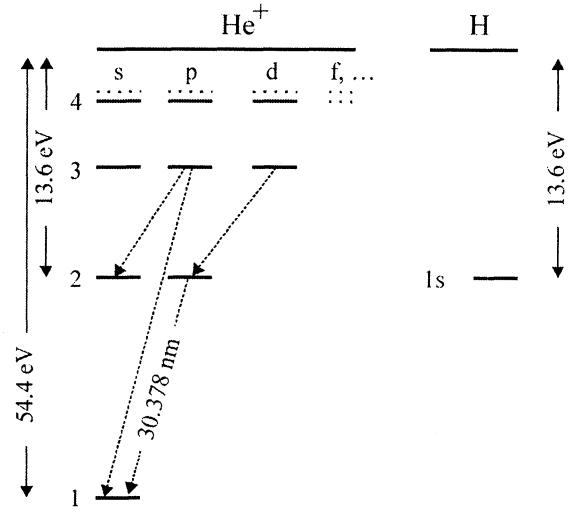

Figure 1. Electron levels in He^+ ions and H atoms.

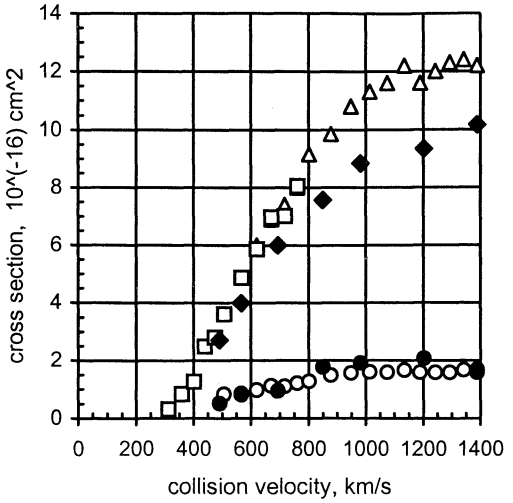

Figure 2. Experimentally determined electron capture cross sections for $He^{2+} + H \rightarrow He^+ + H^+$ collisions. Open squares and open triangles are the (total) cross section of capture in all bound states of He^+ (*Shah and Gilbody* [1978] and *Nutt et al.* [1978], respectively); solid diamonds are the cross section of the collision branches leading to photon emission at 30.4 nm [*Ćirić et al.*, 1985]; and solid and open circles are the cross section for electron capture in $He^+(2s)$ state (*Ćirić et al.* [1985] and *Shah and Gilbody* [1978], respectively).

accidentally resonant charge exchange transfer,

$$He^{2+} + H(1s) \rightarrow He^+(2s \text{ or } 2p) + H^+, \quad (2)$$

has a minimal energy threshold and is the most efficient branch in the He^{2+}-H charge-exchange collisions. For example, only 8% of the products in (1) are He^+ ions in the states other than $He^+(2p)$ or $He^+(2s)$ in 700 km s^{-1} velocity collisions.

Electron capture in the $He^+(2p)$ state is a dominant process in the He^{2+}-H collisions (Figure 2). Electron capture into the higher excited ion states may also lead to the 30.378-nm emission, through a cascade to the ground state via $He^+(2p)$. The cross section of the collisions resulting in the 30.4-nm emission (solid diamonds in Figure 2) is of primary interest for the present work.

The cross section of the charge exchange collisions (equation 2) rapidly increases with the collision velocities. This dependence is exactly opposite to the velocity dependence of the charge exchange in collisions between protons and hydrogen atoms. This difference reflects the nature of the colliding particles, which involves collisions between different particles in the former case and identical particles (symmetric collision) in the latter case.

Alpha particle collisions with hydrogen atoms would also produce helium ions in the $He^+(2s)$ metastable state (Figure 2). The lifetime of these ions is ~1.9 ms, and they reach the ground state by a two-photon emission process [*Shapiro and Breit*, 1959; *Lipeles et al.*, 1965] in the absence of disturbances. The two-photon decay of helium ions does not contribute to the 30.4-nm line emission but is important for the extreme ultraviolet (EUV) background at 1 AU, as discussed in section 7.

3. Solar Wind Emission Model

Let us consider the solar wind 30.4-nm emission as seen from the Earth's orbit on June 3 (point O, Figure 3a). The Earth

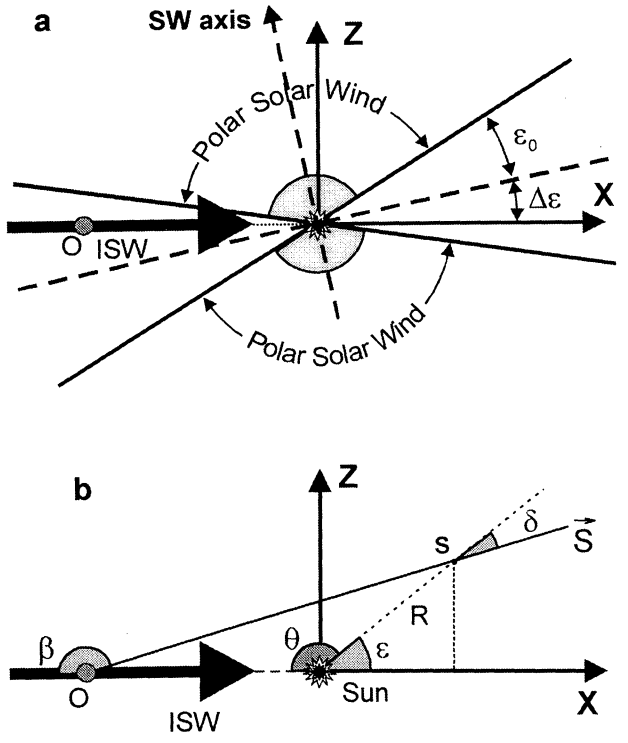

Figure 3. (a) The observer is at point O in the ecliptic plane at 1 AU from the Sun. Interstellar wind (ISW) velocity is parallel to the X axis. Point O is in the exactly upwind direction, which corresponds to the Earth's position on June 3 each year. The X axis is in the ecliptic plane, and the Z axis is normal to the ecliptic. The solar wind axis of symmetry, the "SW axis," is tilted from the normal to the ecliptic by an angle $\Delta\varepsilon$. The slow ecliptic solar wind is confined within the $\pm\varepsilon_0$ angle from the plane (dashed line) normal to the SW axis. The higher latitudes are filled with the fast polar solar wind. (b) The observation direction is described by the angle β counted from the antisolar upwind direction. For a given point S the solar wind type is determined by ecliptic latitude ε, and angle δ determines the Doppler shift of the radiation emitted by the solar wind ions. Angle θ and distance R are the conventional coordinates to describe a point position in the heliosphere with respect to the interstellar wind velocity vector.

is approximately in the so-called upwind direction, the direction from where the interstellar neutral gas (interstellar wind) flows (θ = 0 in Figure 3b.) The upwind direction is ~ 7° off the ecliptic, but we assume that its ecliptic latitude is zero.

Interstellar hydrogen number density distribution in the heliosphere was calculated using the hot model [e.g., *Fahr*, 1974; *Holzer*, 1977; *Meier*, 1977]. This computationally convenient model does not include important plasma-gas coupling in the heliospheric interface. The hot model can be reliably used for many applications if one accounts for the interface effect by "adjusting" the velocity and temperature of the inflowing interstellar gas [*Gruntman*, 1994]. The adjusted parameters are inferred from the observations at 1 AU [e.g., *Costa et al.*, 1999]. The following adjusted interstellar hydrogen parameters are used in this work: number density 0.14 cm^{-3}, temperature 12000 K, bulk velocity 20 km s^{-1}, radiation-to-gravitation force ratio μ=0.8, and ionization rate 6.0×10^{-7} s^{-1} at 1 AU. The ionization rate is inversely proportional to the square of the distance from the Sun and independent of ecliptic latitude and longitude.

We assume that the solar wind consists of two distinct flows, the fast "polar solar wind" and the slow "ecliptic solar wind" (Figure 3a). The solar wind is symmetric about the axis (the "SW axis") tilted from the normal to the ecliptic by an angle $\Delta\varepsilon$. The tilt models the Sun's dipole orientation with respect to the ecliptic. The slow ecliptic solar wind is confined within the $\pm\varepsilon_0$ angle from the plane normal to the SW axis. The higher latitudes are filled with the fast polar solar wind.

Let us consider a photon flux coming to the observation point O from the direction S (Figure 3b). This line of sight is described by the angle β counted from the antisolar upwind direction. A unit volume at a point s=$s(R,\theta)$ along the line of sight would emit 30.4-nm photons at a rate

$$\alpha(s) = n_{He2+}(R,\theta)\, V_{SW}(R,\theta)\, n_H(R,\theta)\, \sigma_{30.4}(V_{SW}), \qquad (3)$$

where n_{He2+} and V_{SW} are the local solar wind alpha particle number density and velocity, respectively; n_H is the local neutral hydrogen number density; $\sigma_{30.4}$ is the velocity-dependent collision cross section leading to the emission of 30.4-nm photons; and R and θ are the conventional coordinates describing the position of a point relative to the interstellar wind vector. Ecliptic latitude ε of the point $s(R,\theta)$ determines the local velocity of the solar wind flow, slow or fast, and correspondingly the cross section.

The solar wind velocity is assumed independent of the heliocentric distance, and the solar wind number density is inversely proportional to the square of the distance from the Sun. The 30.4-nm radiance $F(\alpha)$ (photons cm^{-2} s^{-1} sr^{-1}) at point O is an integral over the line of sight S:

$$F(\alpha) = \frac{1}{4\pi} \int_{\text{Point O}}^{\infty} \alpha(s)\, ds \qquad (4)$$

Since the solar wind number density rapidly decreases with the distance, most of the flux $F(\alpha)$ originates within 10 AU from the Sun (see section 4). Therefore one can disregard the slowing and mass loading of the solar wind due to charge exchange with heliospheric hydrogen and hydrogen photoionization.

Substituting the cross section $\sigma_{30.4}$ in (3) by the cross section σ_{2s} to capture an electron in the $He^+(2s)$ state, one obtains the radiance due to two-photon decay of metastable helium ions. It is necessary to double the radiance (equation 4) because two photons are produced in each decay. The model parameters of the ecliptic and polar solar wind flows at 1 AU are shown in Table 1.

The He^{2+}-H charge exchange cross sections strongly depend on the collision velocity (Figure 2). For example, the cross section $\sigma_{30.4}$ increases by more than a factor of 3 for the velocity increasing from 450 to 750 km s^{-1}. (In contrast, the proton-

Table 1. Assumed Solar Wind Parameters at 1 AU

Solar Wind	Ecliptic	Polar
Proton number density, cm^{-3}	6.5	3.2
Velocity, km s^{-1}	450	750
Solar wind proton flux, cm^{-2} s^{-1}	2.925×10^8	2.40×10^8
Fraction of He^{2+} (by number)	0.045	0.045
$\sigma_{30.4}$, cm^2	2.0×10^{-16}	6.6×10^{-16}
$\sigma_{(2s)}$, cm^2	3.5×10^{-17}	1.2×10^{-16}

hydrogen charge exchange cross section would decrease only by ~20%.) The 30.4-nm emission rate would correspondingly be much higher in the fast polar solar wind than in the ecliptic solar wind. This difference in emission rates opens a way to establish the boundary between the fast and slow solar wind flows from the directional dependence of the radiance $F(\alpha)$.

The proposed solar wind imaging in the 30.4-nm emissions is much more sensitive to the solar wind flow pattern than the measurements of the HI Ly α glow. The solar wind flux varies with the direction and time, which modifies (up to a factor of 2) the ionization rate of interstellar hydrogen in the heliosphere [*Lallement et al.*, 1985; *Bertaux et al.*, 1996; *McComas et al.*, 1999]. The variations of the ionization rate modify the distribution of the heliospheric atomic hydrogen, which is probed through observations of the HI Ly α glow. Most of the glow originates within the ~10-AU distance along the line of sight (the source function), and the hydrogen atom characteristics are affected by the solar gravity and ionization at the distances up to ~20 AU. It takes a few years for an interstellar hydrogen atom to cross such distances with a typical velocity ~ 5 AU yr^{-1}. The solar wind flow properties are inferred from the smoothly varying hydrogen distribution through extensive computer simulations involving a number of model assumptions that introduce uncertainties. Therefore one can establish only the large-scale properties of the solar wind flow averaged over several years, a significant fraction of the 11-year solar cycle, from the HI Ly α glow, and the observed effect is relatively small, less than 20% per year [*Bertaux et al.*, 1999]. In contrast, the proposed imaging in the 30.4-nm emissions would allow one to obtain a high-contrast snapshot of the solar wind flow.

The HI Ly α glow is described approximately by an integral over $n_H(R)/R^2$ with respect to the heliocentric distance R, similar to integral (4). The dependence is actually more complex, since a convolution of the solar line profile and the local hydrogen velocity distribution is under the integral. The simultaneous HI Ly α glow measurements would help interpretations of the proposed 30.4-nm imaging by providing a realistic heliospheric hydrogen distribution.

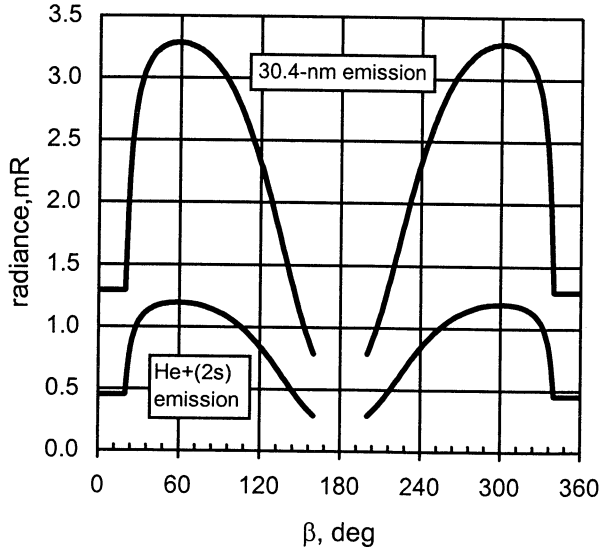

Figure 4. Angular dependence of the 30.4-nm radiance for $\varepsilon_0 = 20°$ and $\Delta\varepsilon = 0$. Directions near $\beta = 0°$ (and 360°) are close to the antisolar direction and confined inside the slow ecliptic solar wind. No points are shown near the 180° direction because of the Sun's proximity. The $He^+(2s)$ two-photon decay emission follows the angular dependence of the 30.4–nm emission.

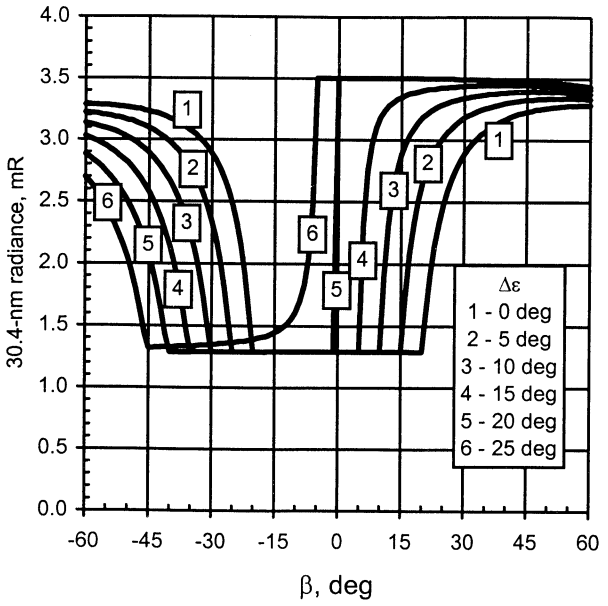

Figure 5. Angular dependence of the 30.4-nm radiance for different tilt angles $\Delta\varepsilon$; $\varepsilon_0 = 20°$.

4. Directional Variation of the 30.4-nm Radiance

Let us assume that the ecliptic solar wind is confined within the ±20° angle from the ecliptic ($\varepsilon_0 = 20°$). Figure 4 shows the calculated 30.4-nm radiance directional dependence for $\Delta\varepsilon = 0$, i.e. for the solar wind symmetric with respect to the ecliptic plane. All observational directions are in the XZ plane normal to the ecliptic (Figure 3). The directions near $\beta = 0°$ (and 360°) are close to the antisolar direction with the line of sight entirely in the slow ecliptic solar wind. With the increasing angle β, the emission intensity would rapidly increase when the line of sight enters the fast polar wind at $\beta > 20°$. The directional dependence $F(\alpha)$ clearly reveals the position of the solar wind flow boundary. No points are shown near the 180° direction because the Sun's proximity would prohibit measurements in this region. The $He^+(2s)$ two-photon decay emission follows the angular dependence of the 30.4–nm emission.

Let us now vary the tilt $\Delta\varepsilon$ of the solar wind axis from 0° to 25°. The upper value would correspond to the observer "submerged" by 5° in the polar solar wind. Figure 5 shows the angular dependences of the 30.4-nm radiance for various tilt angles $\Delta\varepsilon$ and fixed ε_0=20°. For a given observational direction the 30.4-nm radiance would depend on the solar wind tilt axis. A one-dimensional radiance angular distribution, a ~100° swath in the sky, would reveal the fast/slow solar wind flow boundary near the observation point.

The radiance in a given direction depends on the properties of both the solar wind and heliospheric hydrogen along the line of sight. The higher hydrogen number density would translate into more frequent charge exchange collisions and higher 30.4-nm radiance for a given solar wind flux. The distribution of heliospheric hydrogen is essentially nonuniform. The sun is surrounded by the so-called ionization cavity, where hydrogen

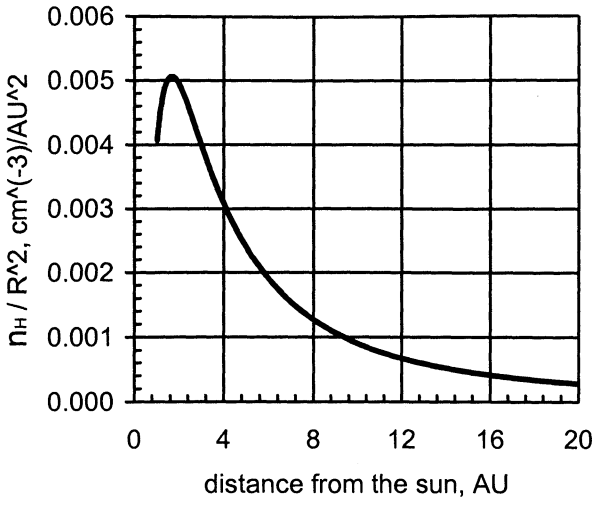

Figure 6. Source function of the 30.4-nm radiance in the upwind direction for an observer at 1 AU.

is depleted by charge exchange and photoionization. The distribution of atomic hydrogen and the strong radial dependence of the solar wind flux would determine the range of the heliocentric distances that effectively contribute to the observed 30.4-nm emission. The radiance source function, i.e., the expression under integral (4), is proportional to $(n_H(R,\theta)/R^2)$. Figure 6 shows the radial dependence of the latter function in the upwind observational direction for an observer at 1 AU (point O in Figure 3).

The source function initially increases with the increasing distance R due to rapid increase of the hydrogen number density. The function peaks at ~3 AU and then decreases. In the downwind hemisphere the function would peak at larger distances because of the extended ionization cavity in that direction. At large distances from the Sun the hydrogen number density is approximately constant with the source function inversely proportional to the square of the heliocentric distance. Most of the radiation observed at 1 AU would originate within ~10 AU from the Sun, which establishes the range of the heliocentric distances probed by imaging of the solar wind.

We demonstrate the main features of solar wind imaging on a simple case of the solar wind with the zero tilt to the ecliptic ($\Delta\varepsilon = 0$) and $\varepsilon_0 = 20°$. Let us position an observer in the ecliptic plane at 1 AU in a point that is $\phi = 60°$ off the upwind direction (Figure 7). An all-sky image of the solar wind in the 30.4-nm emission is shown in Plate 1 (top panel). The angular pixel size is 5°×5°. The vertical coordinate, angle α, is counted from the ecliptic plane. The projection of the observational direction on the ecliptic plane is described by the angle ξ counted from the antisolar direction. The Sun is in the center of the sky image at $\alpha=0$ and $\xi=180°$.

To be precise, only the emissions produced by the solar wind plasma moving away from the observer are shown in Plate 1. Such emissions are red-shifted from the transition wavelength. The emissions of the solar wind plasma moving toward the observer (blue-shifted emissions) appear only for the lines of sight pointed inside the Earth's orbit (i.e., $\beta > 90°$ in Figure 3b, and $90°<\xi<270°$ in Figure 7). Such blue-shifted emissions would peak at the lines of sight close to the Sun as seen from an observational point in the upwind direction. The maximum expected blue-shifted radiance is ~ 0.06 mR, which is 1.5-2 orders of magnitude smaller than the expected red-shifted radiance. We will disregard the blue-shifted emissions.

The sky image (Plate 1, top panel) shows the essential features of the three-dimensional solar wind. The region of the diminished radiance within ±20° from the ecliptic plane ($\alpha=0$), the darker band, corresponds to the slow ecliptic solar wind. The tilt of the Sun's rotation axis with respect to the ecliptic would "twist" this band and make it look sinusoidal with a 360° period along the angle ξ axis. The Sun's rotation would add an extra wavy structure with the varying period along the ξ axis.

The asymmetry of the heliospheric hydrogen distribution modifies the otherwise symmetric emission pattern of the solar wind. The solar wind in the upwind hemisphere would emit more radiation than in the downwind hemisphere, because of the higher hydrogen number densities. The regions of enhanced brightness are prominent for the lines of sight in the upwind hemisphere (angles $200° < \xi < 300°$) in both the polar and ecliptic flow regions. The extended hydrogen ionization cavity in the downwind hemisphere explains the radiance decrease in the $90° < \xi < 160°$ region. The solar wind structure on the far side of the Sun can be clearly seen from 1 AU, allowing one to obtain a truly global 4π-snapshot of the three-dimensional solar wind. Such imaging capabilities would be limited in practice by the closest to the Sun angle, at which one can point the instrument.

The proposed technique would actually image the properties of the solar wind alpha-particle flow, because it is the charge exchange of alpha particles that produces the 30.4-nm emission. The alpha-particle fraction in the solar wind varies with the direction and time [*Borrini et al.*, 1981, 1982; *Barraclough et al.*, 1996; *Bochsler*, 1998; *Bavassano et al.*, 1998; *McComas et al.*, 2000a]; in particular, the coronal mass ejections are being enriched in helium. The alpha-particle fraction in the slow wind is, on average, smaller, 0.01-0.02, than that in the fast solar wind. This smaller helium fraction in the slow solar wind could significantly enhance the contrast of the all-sky 30.4-nm emission maps (Plate 1). The effects of the varying alpha-particle fraction on the global images require further study. However, the major features of these effects can be identified by simple scaling of the emission sky maps (Plate 1). The all-sky maps with high angular resolution would allow the study of the important helium fractional variations [e.g., *Bochsler*, 1998] in the solar wind.

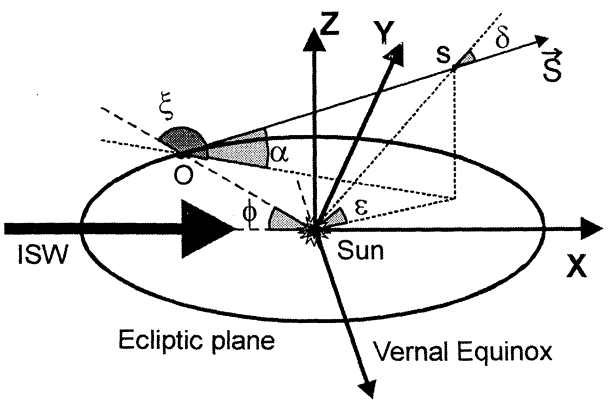

Figure 7. Observation geometry for a simulated all-sky image at 30.4-nm. The observation point is $\phi=60°$ from the upwind direction in the ecliptic plane at 1 AU from the Sun. The angle α is counted from the ecliptic plane; the angle ξ is in the ecliptic plane and counted from the antisolar direction.

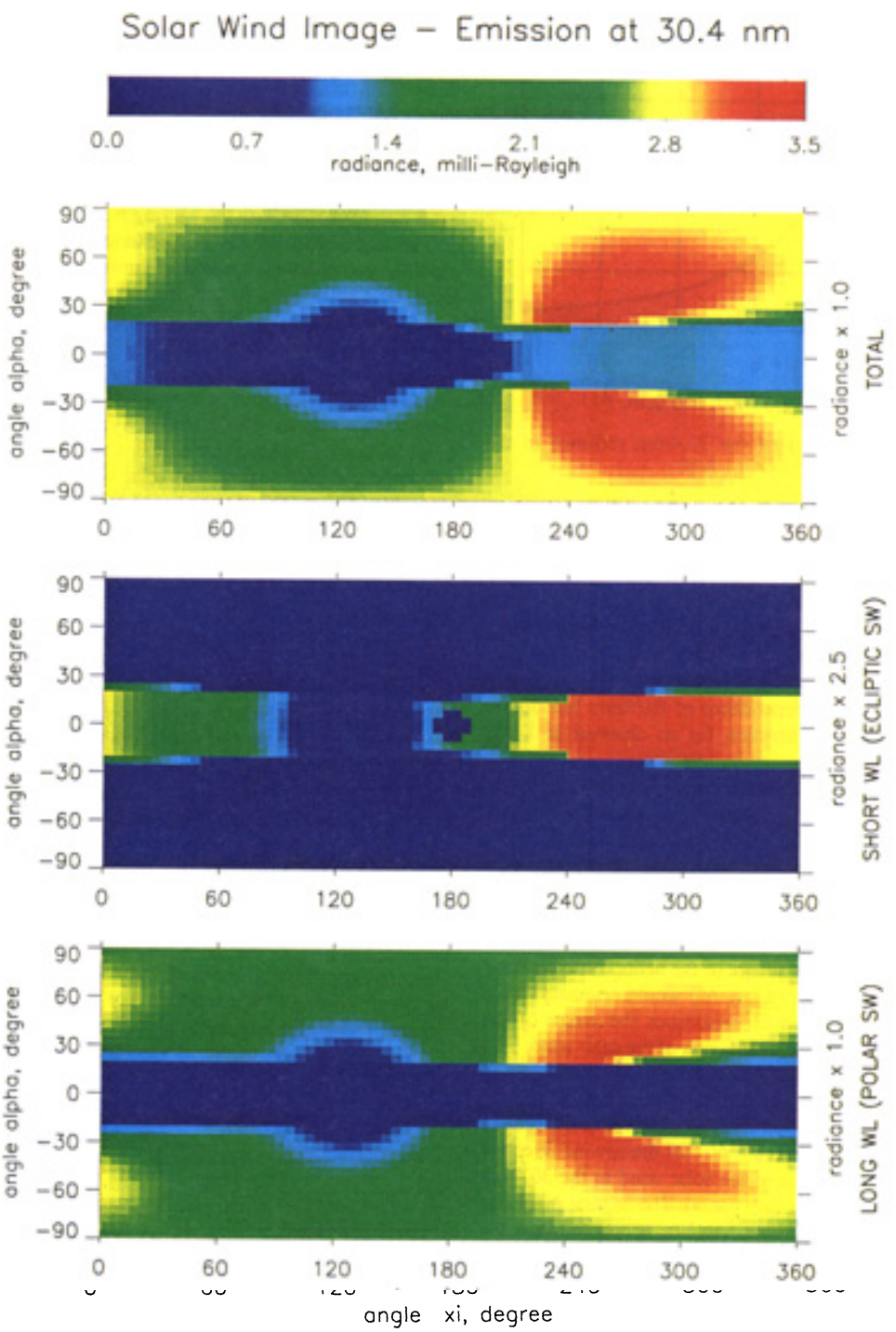

Plate 1. All-sky image in the solar wind 30-4-nm emission. An observer is 60° from the upwind direction in the ecliptic plane at 1 AU from the Sun (point O in Figure 7). The angular pixel size is 5°×5°. Angle α (alpha) is measured from the ecliptic plane. Angle ξ (xi) is counted from the antisolar direction. The Sun is in the center of the sky image at α=0 and ξ=180° (pixels with zero intensity; the Sun would prohibit observations in this direction). (top) Total red-shifted solar wind emission (solar wind moving from an observer). (middle) Sky map in the spectral range corresponding to the solar wind velocity range (along the line of site) 250-550 km s^{-1} (ecliptic solar wind). (bottom) Sky map in the spectral range corresponding to the solar wind velocity range (along the line of site) 550-900 km s^{-1} (polar solar wind). Note that the radiance in the middle panel was multiplied by a coefficient of 2.5 to fit into the same color scale. The radiation in the top panel is the sum of contributions shown in the middle and bottom panels. The total blue-shifted radiance does not exceed 0.06 mR and is disregarded in sky maps.

Alpha-particle velocities are usually higher than the bulk of the solar wind plasma, with the streaming not exceeding the local Alfven speed [*Asbridge et al.*, 1976; *Marsch et al.*, 1982]. Most of the 30.4-nm emissions originate at distances 2-10 AU from the Sun (Figure 6), therefore the streaming would not exceed 20-30 km s^{-1} and produce only a minor effect on the observed radiance and its spectral properties.

5. Background Radiation at 30.4 nm

The feasibility of solar wind imaging depends on the spectral properties and relative strength of the background radiation. Four main sources contribute to the background radiation at 30.4 nm: diffuse galactic background, stellar radiation field, glow of interstellar plasma beyond the heliopause, and glow of the solar wind pickup ions. The galactic EUV radiation field consists of the radiation emitted by the stars (stellar radiation field) and the radiation emitted by hot interstellar plasmas. The stellar radiation dominates the EUV continuum background at wavelengths larger than ~20 nm [*Cheng and Bruhweiler*, 1990; *Vallerga*, 1998]. At shorter wavelengths the emissions of hot interstellar plasma are more important.

The stellar radiation field is a continuum with negligible line emissions, while hot plasmas emit a continuum with prominent line emissions. *Vallerga* [1998] recently reevaluated the stellar radiation field using the most complete database obtained by Extreme Ultraviolet Explorer. He estimates the total (at least 90% complete) radiation field as ~13.5 photon cm^{-2} s^{-1} nm^{-1} around 30 nm. Most of this radiation is produced by a few hot white dwarfs. Consequently, the stellar background is much smaller than average in the directions other than toward these few bright sources [*Gruntman*, 2001]. For isotropic background the stellar radiation field obtained by *Vallerga* [1998] translates into the ~1.3×10^{-2} mR nm^{-1} spectral radiance.

High-temperature (10^5 – 10^7 K) dilute interstellar plasmas efficiently emit EUV radiation that includes both the line emissions and continuum. The line emissions (bound-bound transitions) are due mostly to electron impact excitation with some contribution of recombination processes. The continuum radiation is produced by bremsstrahlung (free-free transition), radiative recombination (free-bound transitions), and two-photon decay of metastable ions.

The growing evidence [*Lallement and Bertin*, 1992; *Lallement et al.*, 1995; *Frisch*, 1995; *Linsky et al.*, 2000] suggests that the Sun is imbedded in a small, several parsecs long, and relatively dense (~ 0.1 cm^{-3}) Local Interstellar Cloud, sometimes called the local fluff. The cloud is too cold (7000-8000 K) to emit EUV radiation. Local Interstellar Cloud is surrounded by a region filled with hot (~10^6 K) and rarefied (~0.005 cm^{-3}) plasmas. This region, called Local Bubble, may extend up to 200 pc in some directions and even expand into the galactic halo. We begin only now to map the contours of Local Bubble [*Sfeir et al.*, 1999; *Welsh et al.*, 1999]. The hot plasmas have probably been heated by nearby supernovae with the resulting deviations from thermodynamic equilibrium and cosmic abundances [e.g., *Cox and Reynolds*, 1987].

The intensity of the EUV radiation field at the Earth is proportional to the integral of the square of the plasma number density along the line of sight, called the emission measure (EM),

$$\mathrm{EM} = \int n_e^2 \, dl . \qquad (5)$$

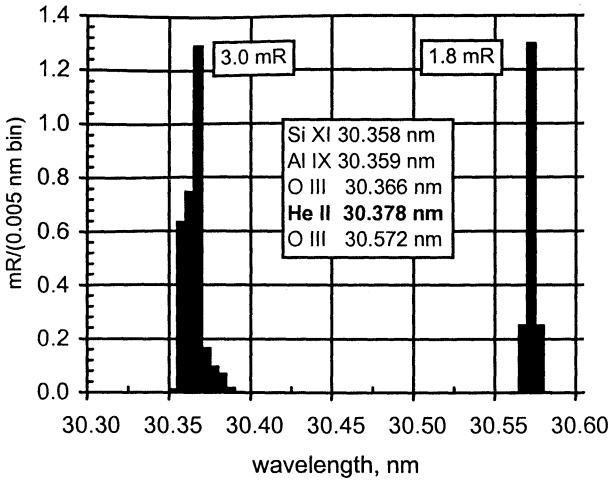

Figure 8. Spectral radiance of the interstellar (Local Bubble) background near 30.4 nm summed over 0.005-nm (0.05-Å) bins. Total radiance of the "left" and "right" peaks is 3.0 and 1.8 mR, respectively. The continuum due to hot plasma emission and stellar sources is ~3.4×10^{-6} mR/(0.005 nm) and ~6.5×10^{-5} mR/(0.005 nm), respectively.

The Local Bubble EUV radiation is attenuated (absorbed) by the passage through neutral atomic hydrogen in Local Interstellar Cloud. Absorption in another nearby cloud, G-cloud [e.g., *Lallement et al.*, 1990], is also important for some directions. The emission measure directional dependence and amount of absorbing interstellar hydrogen (hydrogen slab) are not well known independently. The best recent estimates put the limit on the emission measure, EM = 0.0006 cm^{-6} pc for a 10^{18}-cm^{-2} column density of absorbing hydrogen [*Jelinsky et al.*, 1995].

The isotropic EUV radiation background due to the Local Bubble hot plasma was calculated using the standard model of *Landini and Monsignori-Fossi* [1990]. The plasma was assumed optically thin with the temperature 10^6 K, emission measure EM = 0.0006 cm^{-6} pc, absorbing hydrogen slab column density 10^{18} cm^{-2}, and Maxwellian velocity distribution of the plasma ions.

The calculated background spectral radiance at 30.4 nm, summed over 0.005-nm (0.05-Å) bins, is shown in Figure 8. Most of the line radiation near the 30.378-nm He^+ transition wavelength is produced by interstellar plasma O III (30.366 nm), Al IX (30.359 nm), and Si XI (30.358 nm) lines. The intensities of these three lines are 8, 2, and 1.8 times, respectively, larger than the intensity of the interstellar He II 30.378-nm line. The plasma emission continuum radiation is ~3.4×10^{-6} mR/(0.005 nm), and the stellar radiation field is ~6.5×10^{-5} mR/(0.005 nm).

Single-charged helium ions in the Sun's vicinity would produce glow by scattering the solar 30.4-nm line radiation. Two major populations of He^+ ions would contribute to such glow. First, there are helium ions in the plasma of the local interstellar medium surrounding the solar system. This plasma cannot penetrate the heliosphere and flows around the heliopause, a boundary separating the solar wind and interstellar plasmas. We do not know exactly the distance to the heliopause and its shape [e.g., *Gruntman*, 2001]. The estimates suggest that the heliopause could be somewhere between 120 and 160 AU in the upwind direction and farther away in other directions.

Second, there are single-charged helium pickup ions in the solar wind. Interstellar helium atoms are ionized in interplanetary space and picked up by the solar wind plasma flow. The origin of the helium pickup ions is well understood, and their properties are extensively studied experimentally [e.g., *Moebius et al.*, 1985; *Gloeckler*, 1996; *Moebius*, 1996].

Gruntman and Fahr [1998, 2000] considered the glow of single-charged oxygen ions in the Sun's vicinity. Similar to helium, oxygen ions are present in the local interstellar medium and as pickup ions in the solar wind. Conceptually, the oxygen ion glow is similar to the glow of the helium ions with the differences in ionization rates, cross sections, and solar line intensities and spectral profiles. The method and details of the ion glow calculations can be found in the work of *Gruntman and Fahr* [2000]. Mapping the helium and oxygen ion glow, combined with the complementary heliosphere imaging in energetic neutral atom fluxes [*Gruntman*, 1997; *Gruntman et al.*, 2001], would establish the three-dimensional structure of the heliospheric interface region.

The results of the calculations of the helium ion glow at 30.4 nm are presented elsewhere [*Gruntman*, 2001]. The expected LISM plasma glow smoothly varies across the sky and peaks in the upwind direction with the maximum radiance of ~11 mR. This glow is sometimes called the "heliopause glow" because its mapping would establish the distance to and shape of the heliopause. The glow of the helium pickup ions sharply peaks in the downwind direction with the radiance ~16 mR. To summarize, the helium ion glow would be spectrally separate (see Section 6) from and a factor of 3-5 brighter than the solar wind charge exchange emissions.

6. Spectral Properties of the 30.4-nm Radiation

The 30.4-nm radiation emitted by the solar wind He^+ ions would be Doppler-shifted, which opens a way of determining the solar wind speed directly from spectroscopic measurements of the solar wind emissions. The solar wind velocity and the angle δ (Figure 3b) between the line of sight and the velocity vector determine the Doppler shift. The angle δ rapidly approaches zero with the increasing distance from the observation point. For observation angles $\beta < 90°$ (Figure 3b), all the emissions would be red-shifted with the solar wind ions moving from the observer. For $90° < \beta < 270°$ a small fraction of the observed emission would be blue-shifted. Different speeds of the polar and ecliptic solar wind flows would result in different Doppler shifts. A Doppler shift of 0.005 nm (0.05 Å) would correspond to the radial velocity increment of ~50 km s^{-1}.

A combined spectral distribution from all sources of radiation is shown in Figure 9 for an observational direction $\beta=25°$ from the upwind direction. The observer is in the upwind direction at 1 AU (Figure 3b). The solar wind is symmetric with respect to the ecliptic plane ($\Delta\varepsilon=0°$) and $\varepsilon_0=20°$. The solar wind emission consists of two distinct peaks, a "short-wavelength" peak produced by the slow ecliptic solar wind and a more red-shifted "long-wavelength" peak produced by the fast polar solar wind. Both solar wind peaks are clearly separate from the heliopause glow, the glow of the pickup ions in the solar wind, and the line emissions of the Local Bubble interstellar plasma. The combined continuum radiation, $<10^{-4}$ mR/(0.005 nm), is negligible.

The spectral properties of the ion glow under solar illumination are essentially different from those of emissions originating in the solar wind. The glow is largely determined by the spectral properties of the illuminating source, i.e., the width of the solar line. (We used the solar 30.4-nm line with full width at half maximum (FWHM) 0.01 nm [*Doschek et al.*, 1974] in our calculations.) The ions with the radial velocities outside the line do not scatter solar radiation. This explains why the spectral properties of the (relatively cold) LISM ion glow are not unlike those of the pickup ions with a very wide velocity distribution. The glow is concentrated at the solar line and clearly separated from the solar wind charge exchange emissions, the latter being substantially Doppler-shifted from the transition wavelength.

The radiance of the LISM plasma and pickup ion glow would smoothly vary in the 6-20 mR range across the sky [*Gruntman*, 2001]. This radiance is significantly larger than the expected 3-mR radiance (Figure 9) of the interstellar background at 30.4 nm. Heliopause EUV imaging at "low" resolution, 0.025 nm (0.25 Å), would reliably separate the solar

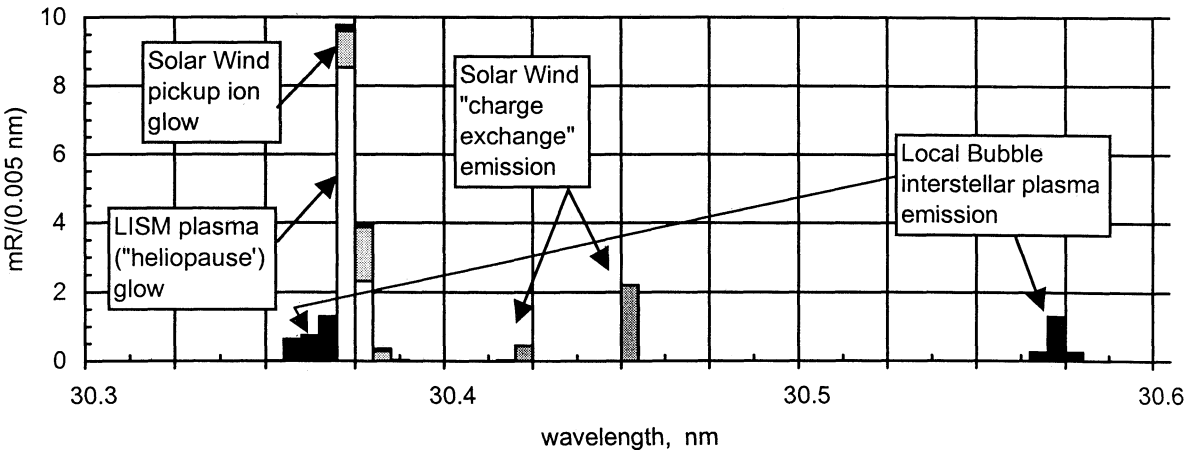

Figure 9. Combined spectral radiance summed over 0.005-nm (0.05-Å) bins from all sources of radiation for an observational direction 25° from the upwind direction; the observer is in the upwind direction at 1 AU from the Sun. Solid bars indicate Local Bubble interstellar plasma emission; dark shaded bars indicate two peaks of the solar wind charge exchange emission; light shaded bars indicate solar wind pickup ion glow; and open bars indicate local interstellar medium plasma ("heliopause") glow. The solar wind emission consists of two distinct peaks, one produced

wind emissions from the ion glow and interstellar background. The ion glow map would image the heliopause and determine the asymmetry of the interstellar magnetic field and the ionization state of helium in the local interstellar medium [*Gruntman and Fahr*, 1998, 2000; *Gruntman*, 2001].

The fast and slow solar wind flows would not be spectrally resolved in imaging with the low spectral resolution. However, the emission brightness, as shown in Figures 4 and 5, is sensitive to the solar wind velocities and to the distance to and shape of the boundary between the solar wind flows. Therefore low spectral resolution imaging would establish the main properties of the three-dimensional solar wind.

Imaging with "high" spectral resolution, 0.005 nm (0.05 Å), would dramatically increase the science return of the solar wind imaging experiment. First, such a resolution would separate the interstellar plasma line background from the LISM ion and solar wind pickup ion glows (Figure 9). Consequently, "clean" background-free imaging of the heliopause would become possible. Note that the alpha particle streaming with respect to the solar wind flow is smaller than the velocity that can be resolved by the high spectral resolution mode.

Second, the two solar wind components, fast and slow, would be clearly separated as the short- and long-wavelength peaks. Angular dependences of the intensities in these two peaks are much stronger and show more details than the angular dependence of the total, combined solar wind emissions. We define here the short-wavelength and long-wavelength radiation peaks as those corresponding to the solar wind flows with the velocities (along the line of sight) in the 250-550 and 550-900 km s^{-1} ranges, respectively. The radiance directional dependences for these two velocity (spectral) ranges along a swath in the sky, as in Figures 3 and 4, are shown in Figure 10. At small angles β all the emission is produced by the slow ecliptic solar wind, while at higher β the fast solar wind dominates the radiance. The $20°<\beta<35°$ region with large directional gradients of the emissions is most important for diagnostics of the flow boundary.

All-sky images of the solar wind emissions for the short-wavelength and long-wavelength spectral ranges are shown in the middle and bottom panels of Plate 1, respectively. These images correspond to the emissions originating in the slow and fast solar wind flows. Note that the radiance in the middle panel is multiplied by a coefficient 2.5 to fit into the same color scale. It is important that the solar wind properties can be efficiently explored in the regions on the far side of the Sun and over the Sun's poles.

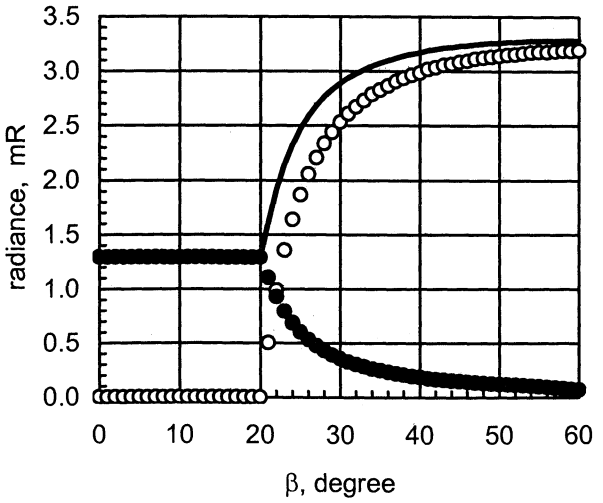

Figure 10. Angular dependence of the 30.4-nm radiance for $\varepsilon_0 = 20°$ and $\Delta\varepsilon = 0$: solid circles indicate short-wavelength peak (slow solar wind); open circles indicate long-wavelength peak (fast solar wind); and solid line indicates total radiation (also shown in Figure 4).

Imaging with high spectral resolution would directly establish the local solar wind velocities through the Doppler shifts. A spectral resolution of 0.005 nm (0.05 Å) translates into a 50 km s^{-1} velocity resolution. It may also be possible to directly observe the propagation of coronal mass ejections (CMEs) practically anywhere in the heliosphere. The CMEs could be followed, with their velocity evolution monitored, as they move through the heliosphere up to distances of 5-10 AU. The space mission, experiment, and instrumentation for imaging of the three-dimensional solar wind are beyond the scope of this article. We note only that a spectrometer with the sensitivity better than 1 mR and the spectral resolution 0.025 nm (0.25 Å) for low-resolution imaging or 0.005 nm (0.05 Å) for high-resolution imaging is required. The spectral resolution requirement rules out the use of broadband photometers, similar to a powerful 30.4-nm imager (FWHM $\Delta\lambda \sim 4$ nm) on the recently launched Imager for Magnetosphere-to-Aurora Global Exploration (IMAGE) mission [*Sandel et al.*, 2000]. The Earth geocorona dayglow is a few Rayleighs at 30.4 nm [e.g., *Meier*, 1991], and too many photons would reach the nightside through multiple scattering. This bright radiation thwarted the past attempts to detect extraterrestrial signatures at 30.4 nm from sounding rockets and low-Earth orbit spacecraft [e.g., *Tohmatsu*, 1970; *Meier and Weller*, 1972; *Paresce et al.*, 1973, 1983; *Weller and Meier*, 1974; *Chakrabarti et al.*, 1982]. Imaging of the solar wind can only be performed from a spacecraft outside the geocorona and magnetosphere.

The instrument throughput providing the ability to accumulate the statistically significant number of photon counts in the desired time intervals is the major challenge for instrumentation development. Real-time monitoring of the fast/slow solar wind flow boundary in support of near-Earth in situ measurements would require imaging of a one-dimensional swath in the sky with ~ 20 3°×3° pixels. The measurement of one pixel in 30 min would allow the flow boundary monitoring on a 10-hour basis.

The full sky contains ~1600 5°×5° angular (directional) pixels. Obtaining an all-sky image during a time interval shorter than the period of the sun's rotation, for example during a week, would require the measurement of one angular pixel in ~400 s. Since not all the observational directions are of equal importance, one may possibly require ~1000-s accumulation for each angular pixel/direction. A multipixel instrument would ease this requirement, allowing proportionally higher accumulation times. The recently developed EUV spectrometers have significantly advanced the art of diffuse EUV radiation detection, achieving the sensitivity of ~ 10 mR nm^{-1} (1 mR $Å^{-1}$) [*Bowyer et al.*, 1997]. The new space mission, Cosmic Hot Interstellar Plasma Spectrometer (CHIPS), currently under preparation, will study the diffuse galactic radiation with the sensitivity ~ 1 mR/line at $\lambda<26$ nm. Imaging of the solar wind requires further 1-3 orders of magnitude improvement in instrument spectral resolution and throughput. This is a challenging but not impossible task.

7. EUV Background Due to Two-Photon Decay at 1 AU

Metastable $He^+(2s)$ ions of the solar wind would be born in charge exchange collisions (equation 2). Two-photon decay of these ions would contribute to the EUV continuum background. The upper limit of the background was recently obtained by *Lieu et al.* [1993] and *Jelinsky et al.* [1995]. The solar wind contribution needs to be quantified because of its importance for interpretation of the galactic background measurements at 1 AU.

Metastable helium ions undergo two-photon decay with the rate ~526 s^{-1} (lifetime 1.9 ms) [*Shapiro and Breit*, 1959]. Collisional and radiative processes may also depopulate (quench) the newly formed solar wind $He^+(2s)$ ions. *Gruntman* [1990] discussed the relevant physical processes in detail for a similar case of metastable atomic hydrogen in the solar system.

Metastable helium ions can be depopulated by photoionization, photon excitation to higher electronic levels, solar wind electron and proton impact ionization, and transition to nonmetastable $He^+(2p)$ state by collisions with the solar wind electrons and protons. The photoionization rate of $He^+(2s)$ metastable ions is ~3.1×10^{-8} s^{-1} at 1 AU at solar minimum (the solar EUV spectrum of *Hall et al.* [1985] was used in the calculations), and the photoexcitation rate is ~ 3.1×10^{-5} s^{-1}.

The most efficient collision processes depopulating the metastable ($2S$) states are those leading to the ($2P$) states [*Gruntman*, 1990]. Applying the formalism developed by *Purcell* [1952], one can show that the $He^+(2s)$ depopulation rates would be ~1×10^{-4} and ~3×10^{-4} s^{-1} at 1 AU for collisions with the solar wind electrons and protons, respectively. The depopulation rates due to solar photons and collisions with the solar wind electrons and ions are roughly inversely proportional to the square of the heliocentric distance.

Solar wind alpha particles move with the velocity measurably different from that of the bulk of the solar wind [e.g., *Asbridge et al.*, 1976; *Marsch et al.*, 1982, *McComas et al.*, 2000a]. This relative streaming combined with the alpha-particle thermal motion and recoil during the change exchange collisions with hydrogen atoms would result in motion of the newly born metastable $He^+(2s)$ ions with respect to the bulk of the solar wind plasma and, correspondingly, with respect to the frozen-in magnetic field. A particle moving relative to the magnetic field would "see" the electric field $E \sim (1/c)VB$, where B is the magnetic field component normal to the ion velocity vector. *Bethe and Salpeter* [1977] gave a convenient numerical expression for the depopulation rate of metastable hydrogen atoms through transition to the ($2P$) state (rapidly followed by a transition to the ground state) due to small electric fields. For metastable helium ions, the depopulation rate r_B (s^{-1}) would be

$$r_E = r_{2P} \times \left(E/6312\right)^2 \qquad (6)$$

where $r_{2P} = 1.0\times10^{10}$ s^{-1} is the transition rate from the $He^+(2p)$ state to the ground state and E is in the units of V cm^{-1}. Most of the two-photon decay emissions originate at distances 2-10 AU from the Sun (Figure 6) with the interplanetary magnetic field $<10^{-8}$ T (10 γ) and alpha particles streaming capped by the local Alfven speed [*Asbridge et al.*, 1976; *Marsch et al.*, 1982], as confirmed by the Ulysses measurements across the large range of latitudes [*McComas et al.*, 2000a]. Even for such a large relative velocity as 100 km s^{-1} and large magnetic field as 10^{-8} T (10 γ), the depopulation rate r_E would not exceed 2×10^{-7} s^{-1} at 1 AU.

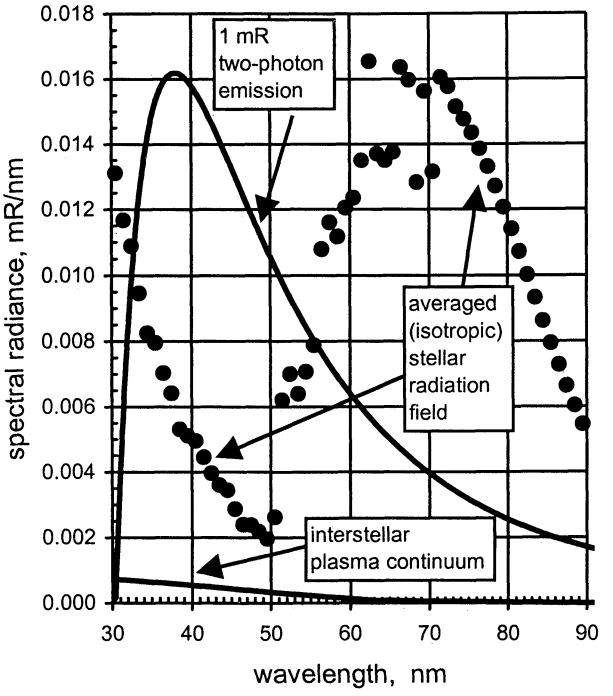

Figure 11. Spectral distribution of the 1-mR solar wind radiance due to two-photon decay of metastable helium ions. Also shown are the Local Bubble hot plasma continuum (lower solid curve) and the average isotropic stellar radiation field (solid circles) obtained by *Vallerga* [1998].

The total depopulation rate of the $He^+(2s)$ ions is several orders of magnitude smaller than the two-photon decay rate. Therefore one can assume that practically all helium metastable ions born in charge exchange of the solar wind alpha particles would undergo two-photon decay. The radiance of this emission would vary over the sky in the 0.4-1.2 mR range (Figure 4). *Spitzer and Greenstein* [1951] calculated the spectral distribution of two-photon decay, and *Tucker and Koren* [1971] suggested a convenient analytical approximation of the spectral shape.

The calculated spectral distribution of the 1-mR solar wind radiance due to two-photon decay is shown in Figure 11 for the 30-90 nm spectral range. Also shown are the Local Bubble hot plasma continuum and the average isotropic stellar radiation field obtained by *Vallerga* [1998]. Above the 50.4-nm He I edge, the stellar field is dominated by a single source, the nearby B2 II star, ε *Canis Majoris* (Adhara/Adara) [*Vallerga and Welsh*, 1995; *Vallerga*, 1998]. Below this edge, several white dwarfs determine the stellar radiation field [*Vallerga*, 1998]. One can see that the two-photon emission of metastable helium ion in the solar wind would dominate the sky brightness in most directions (except those toward the few bright sources) in the 30-90 nm spectral range.

Acknowledgments. The work was partially supported by a NASA grant. Janet G. Luhmann thanks Wayne Pryor and Rosine Lallement for their assistance in evaluating this paper.

References

Asbridge, J.R., S.J. Bame, W.C. Feldman, and M.D. Montgomery, Helium and hydrogen velocity differences in the solar wind, *J. Geophys. Res.*, *81*, 2719-2727, 1976.

Barraclough, B. L., W.C. Feldman, J.T. Gosling, D.J. McComas, and J.L. Phillips, He abundance in the solar wind: Observations from the Ulysses, in *Solar Wind 8, AIP Conf. Proc., 382*, 277-280, 1996.

Bavassano, B., R. Bruno, and E. Pietropaolo, The solar wind alpha-particle content as a clue for the origin of the solar flows, *Geophys. Res. Lett., 25*, 2921-2924, 1998.

Bertaux, J.L., E. Quemerais, and R. Lallement, Observation of a sky Lyman α groove related to enhanced solar wind mass flux in the neutral sheet, *Geophys. Res. Lett., 23*, 3675-3678, 1996.

Bertaux, J.-L., E. Kyrölä, E. Quemerais, R. Lallement, W. Schmidt, T. Summanen, J. Costa, and T. Mäkinen, SWAN observations of the solar wind latitude distribution and its evolution since launch, *Space Sci. Rev., 87*, 129-132, 1999.

Bethe, H.A., and E.E. Salpeter, *Quantum Mechanics of One- and Two-Electron Atoms*, Plenum, New York, 1977.

Bochsler, P., Structure of the solar wind and compositional variations, *Space Sci. Rev., 85*, 291-302, 1998.

Borrini, G., J.T. Gosling, S.J. Bame, W.C. Feldman, and J.M. Wilcox, Solar wind helium and hydrogen structure near the heliospheric current sheet: A signal of coronal streamers at 1 AU, *J. Geophys. Res., 86*, 4565-4573, 1981.

Borrini, G., J.T. Gosling, S.J. Bame, and W.C. Feldman, Helium abundance enhancement in the solar wind, *J. Geophys. Res., 87*, 7370-7378, 1982.

Bowyer, S., J. Edelstein, and M. Lampton, Very high sensitivity extreme ultraviolet spectrometer for diffuse radiation, *Astrophys. J., 485*, 523-532, 1997.

Chakrabarti, S., F. Paresce, S. Bowyer, Y. T. Chiu, and A. Aikin, Plasmaspheric helium ion distribution from satellite observations of HeII 304-Å, *Geophys. Res. Lett., 9*, 151-154, 1982.

Cheng, K.-P., and F.C. Bruhweiler, Ionization processes in the local interstellar medium: Effects of the hot coronal substrate, *Astrophys. J., 364*, 573-581, 1990.

Ćirić, D., D. Dijkkamp, E. Vlieg, and F.J. de Heer, Selective electron capture into He II(n,l) subshells in collisions of He^{2+} with atomic and molecular hydrogen, *J. Phys. B., 18*, 4745-4762, 1985.

Costa, J., R. Lallement, E. Quémerais, J.-L. Bertaux, E. Kyrölä, and W. Schmidt, Heliospheric interstellar H temperature from SOHO/SWAN H cell data, *Astron. Astrophys., 349*, 660-672, 1999.

Cox, D.P., and R.J. Reynolds, The local interstellar medium, *Annu. Rev. Astron. Astrophys., 25*, 303-344, 1987.

Doschek, G.A., W.E. Behring, and U. Feldman, The widths of the solar He I and He II lines at 584, 537, and 304 Å, *Astrophys. J., 190*, L141-L142, 1974.

Fahr, H. J., The extraterrestrial UV-background and the nearby interstellar medium, *Space Sci. Rev., 15*, 483-540, 1974.

Frisch, P. C., Characteristics of nearby interstellar medium, *Space Sci. Rev., 72*, 499-592, 1995.

Gloeckler, G., The abundance of atomic ^{1}H, ^{4}He and ^{3}He in the local interstellar cloud from pickup ion observations with SWICS on Ulysses, *Space Sci. Rev., 78*, 335-346, 1996.

Gruntman, M.A., Two-step photoionization of hydrogen atoms in interplanetary space, *Planet. Space Sci.,38*, 1225-1230, 1990.

Gruntman, M.A., Charge-exchange born He^+ ions in the solar wind, *Geophys. Res. Lett., 19*, 1323-1326, 1992.

Gruntman, M.A., Neutral solar wind properties: Advance warning of major geomagnetic storms, *J. Geophys. Res., 99*, 19,213-19,227, 1994.

Gruntman, M., Energetic neutral atom imaging of space plasmas, *Rev. Sci. Instrum., 68*, 3617-3656, 1997.

Gruntman, M., Mapping the heliopause in EUV, in *Proceedings of the COSPAR Colloquium on the Physics of the Outer Heliosphere*, Elsevier Sci., New York, in press, 2001.

Gruntman, M., and H.J. Fahr, Access to the heliospheric boundary: EUV-echoes from the heliopause, *Geophys. Res. Lett., 25*, 1261-1264, 1998.

Gruntman, M., and H.J. Fahr, Heliopause imaging in EUV: Oxygen O^+ ion 83.4-nm resonance line emission, *J. Geophys. Res., 105*, 5189-5200, 2000.

Gruntman, M., E.C. Roelof, D.G. Mitchell, H.J. Fahr, H.O. Funsten, D.J. McComas, Energetic neutral atom imaging of the heliospheric boundary region, *J. Geophys. Res.*, in press, 2001.

Hall, L.A., L.J. Heroux, and H.E. Hinteregger, Solar ultraviolet irradiance, in *Handbook of Geophysics and the Space Environment*, edited by A.S. Jursa, pp. (2-1)-(2-21), Air Force Geophys. Lab., 1985.

Holzer, T. E., Neutral hydrogen in interplanetary space, *Rev. Geophys., 15*, 467-490, 1977.

Jelinsky, P., J.V. Vallerga, and J. Edelstein, First spectral observations of the diffuse background with the *Extreme Ultraviolet Explorer*, *Astrophys. J., 442*, 653-661, 1995.

Kyrölä, E., T. Summanen, W. Schmidt, T. Mäkinen, E. Quemerais, J.-L. Bertaux, R. Lallement, and J. Costa, Preliminary retrieval of solar wind latitude distribution from Solar Wind Anisotropies/SOHO observations, *J. Geophys. Res., 103*, 14,523-14,538, 1998.

Lallement, R., and P. Bertin, Northern-hemisphere observations of nearby interstellar gas: possible detection of the local cloud, *Astron. Astrophys.*, 266, 479-485, 1992.

Lallement, R., J.-L. Bertaux, and V.G. Kurt, Solar wind decrease at high heliographic latitudes detected from Prognoz interplanetary Lyman-alpha mapping, *J. Geophys. Res., 90*, 1413-1423, 1985.

Lallement, R., R. Ferret, A. Vidal-Madera, and C. Gray, Velocity structure of the local interstellar medium, in *Physics of the Outer Heliosphere*, edited by S. Grzedzielski and D.E. Page, pp.37-42, Pergamon, Tarrytown, N.Y., 1990.

Lallement, R., R. Ferlet, A.M. Lagrange, M. Lemoine, and A. Vidal-Madjar, Local Cloud structure from HST-GHRS, *Astron. Astrophys., 304*, 461-474, 1995.

Landini, M., and B.C. Monsignori Fossi, The X-UV spectrum of thin plasmas, *Astron. Astrophys. Suppl. Ser., 82*, 229-260, 1990.

Lieu, R., S. Bowyer, M. Lampton, P. Jelinsky, and J. Edelstein, *EUVE* first light observation of the diffuse sky background, *Astrophys. J., 417*, L41-L44, 1993.

Linsky, J.L., S. Redfield, B.E. Wood, and N. Piskunov, The three-dimensional structure of the warm; local interstellar medium, I, Methodology, *Astrophys. J., 528*, 756-766, 2000.

Lipeles, M., R. Novick, and N. Tolk, Direct detection of two-photon emission from the metastable state of singly ionized helium, *Phys. Rev. Lett., 15*, 690-693, 1965.

Marsch, E., K.-H. Muhlhauser, H. Rosenbauer, R. Schwenn, and F.M. Neubauer, Solar wind helium ions: Observations of the Helios solar probes between 0.3 and 1.0 AU, *J. Geophys. Res., 87*, 35-51, 1982.

McComas, D.J., H.O. Funsten, J.T. Gosling, and W.R. Pryor, Ulysses measurements of variations in the solar wind-interstellar hydrogen charge exchange rate, *Geophys. Res. Lett., 26*, 2701-2704, 1999.

McComas, D.J., B.L. Barraclough, H.O. Funsten, J.T. Gosling, E. Santiago-Muñoz, R.M. Skoug, B.E. Goldstein, M. Neugebauer, P. Riley, and A. Balogh, Solar wind observations over Ulysses' first full polar orbit, *J. Geophys. Res., 105*, 10,419-10,433, 2000a.

McComas, D.J., J.T. Gosling, and R.M. Skoug, Ulysses observations of the irregularly structured mid-latitude solar wind during the approach to solar maximum, *Geophys. Res. Lett., 27*, 2437-2440, 2000b.

Meier, R.R., Some optical and kinetic properties on the nearby interstellar medium, *Astron. Astrophys., 55*, 211-219, 1977.

Meier, R.R., Ultraviolet spectroscopy and remote sensing of the upper atmosphere, *Space Sci. Rev., 58*, 1-185, 1991.

Meier, R.R. and C.S. Weller, EUV resonance radiation from helium atoms and ions in the geocorona, *J. Geophys. Res., 77*, 1190-1204, 1972.

Moebius, E., The local interstellar medium viewed through pickup ions, recent results and future perspectives, *Space Sci. Rev., 78*, 375-386, 1996.

Moebius, E., et al., Direct observation of He^+ pickup ions of interstellar origin in the solar wind, *Nature, 318*, 426-429, 1985.

Neugebauer, M., The three-dimensional solar wind at solar activity minimum, *Rev. Geophys., 37*, 107-126, 1999.

Nutt, W.L., R.W. McCullough, K. Brady, M.B. Shah, and H.B. Gilbody, Electron capture by He^{2+} ions in collisions with H and H_2 at impact energies below 10 keV, *J. Phys. B: At. Mol. Phys., 11*, 1457-1462, 1978.

Paresce, F., S. Bowyer, and S. Kumar, Observations of the He II 304-A radiation in the night sky, *J. Geophys. Res., 78*, 71-79, 1973.

Paresce, F., H. Fahr, and G. Lay, A search for interplanetary He II, 304-A emission, *J. Geophys. Res., 86*, 10,038-10,048, 1981.

Purcell, E.M., The lifetime of the $2^2S_{1/2}$ state of hydrogen in an ionized atmosphere, *Astrophys. J., 116*, 457-462, 1952.

Sandel, B.R., et al., The extreme ultraviolet imager investigation for the IMAGE mission, *Space Sci. Rev., 91*, 197-242, 2000.

Sfeir, D.M., R. Lallement, F. Crifo, and B.Y. Welsh, Mapping the

contours of the Local bubble: Preliminary results, *Astron. Astrophys.*, *346*, 785-797, 1999.

Shah, M.B., and H.B. Gilbody, Electron capture and $He^+(2s)$ formation in fast He^{2+}-H and He^+-H collisions, *J. Phys. B: At. Mol. Phys.*, *11*, 121-131, 1978.

Shapiro, J., and G. Breit, Metastability of 2s states of hydrogenic atoms, *Phys. Rev.*, *113*, 179-181, 1959.

Spitzer, L., and J. Greenstein, Continuous emission from planetary nebulae, *Astrophys. J.*, *114*, 407-420, 1951.

Tohmatsu, T., The hydrogen and helium ultraviolet glow, its origin and aeronomical significance, *Space Res.*, *X*, 608-622, 1970.

Tucker, W.H., and M. Koren, Radiation from a high-temperature, low-density plasma: The X-ray spectrum of the solar corona, *Astrophys. J.*, *168*, 283-311, 1971.

Vallerga, J., The stellar extreme-ultraviolet radiation field, *Astrophys. J.*, *497*, 921-927, 1998.

Vallerga, J.V., and B.Y. Welsh, ε Canis Majoris and the ionization of the local cloud, *Astrophys. J.*, *444*, 702-707, 1995.

Weller, C.S., and R.R. Meier, First satellite observations of the He^+ 304-Ä radiation and its interpretation, *J. Geophys. Res.*, *79*, 1572-1574, 1974.

Welsh, B.Y., D.M. Sfeir, M.M. Sirk, and R. Lallement, EUV mapping of the local interstellar medium: The Local Chimney revealed?, *Astron. Astrophys.*, *352*, 308-316, 1999.

M. Gruntman, Department of Aerospace and Mechanical Engineering, MC-1191, University of Southern California, Los Angeles, CA 90089-1191. (mikeg@spock.usc.edu)

(Received July 14, 2000; revised September 21, 2000;
accepted September 21, 2000.)